Hydrodynamic interaction between two nonspherical capsules in shear flow

Duc-Vinh Le* and K.-H. Chiam†

*A*STAR Institute of High Performance Computing, 1 Fusionopolis Way, #16-16 Connexis, Singapore 138632, Singapore*

(Received 10 May 2011; published 23 November 2011)

The hydrodynamic interaction between two nonspherical capsules suspended in a simple shear flow is studied numerically using a front-tracking method. The capsules are enclosed by thin shells which develop in-plane tensions and bending moments due to a preferred three-dimensional unstressed configuration. Computations are performed for capsules with spherical, oblate spheroidal, and biconcave unstressed shapes for a wide range of dimensionless shear rates and initial separation distances between the two capsules. The bending modulus and viscosity ratio between the internal and surrounding fluids are chosen to be those of healthy red blood cells. Depending on the initial separation distance, we find that two spherical capsules in shear flow either cross over each other or undergo spiraling motion. In addition, the long-time interaction behavior of capsules also depends strongly on the unstressed shapes. More oblate or biconcave capsules exhibit two additional type of interactions, namely swapping and continuous rotation, which occur only when each capsule undergoes tumbling motion.

DOI: 10.1103/PhysRevE.84.056322 PACS number(s): 47.55.−t, 46.70.−p

I. INTRODUCTION

The dynamics of deformable objects such as liquid droplets, elastic capsules, lipid vesicles, and red blood cells in flows has received growing interest experimentally [1–4], theoretically [5–7], and numerically [8–12] in recent years. This is because of their importance in a wide range of industries such as the pharmaceutical industry as well as in basic physiology, the most relevant of which is blood flow and understanding how its constituents such as red blood cells affect the flow characteristics. Therefore, it is important to understand how multiple cells interact with each other in flows as well as the collective behavior and rheology of a flowing suspension of cells.

The dynamics of a single cell or elastic capsule is relatively well understood. In a simple shear flow, elastic capsules exhibit a stationary tank-treading behavior if the initial unstressed shape is a sphere [8]. For spheroidal or biconcave unstressed shapes such as the red blood cell, transients to a tumbling state can occur. Alternatively, the capsules may undergo swinging motion in which they exhibit periodic oscillations in both deformation and orientation superimposed on a tank-treading mode [13–15]. In addition to the shape of the capsule, the dynamics of the capsule also depends on viscosity ratio between the internal and suspending fluids, applied shear rate, membrane modulus of elasticity, and membrane bending modulus.

However, not much has been studied about the hydrodynamic interaction between capsules. The first study of the hydrodynamic interaction between capsules was investigated by Breyiannis and Pozrikidis [16] who considered a two-dimensional suspension of capsules in shear flow. Three-dimensional situation where two identical spherical capsules interact in simple shear flow was considered by Lac *et al.* [17]. The study was later extended by considering the case where the centers of mass of the spherical capsules are not constrained to be in the same shear plane [18]. It has been found that hydrodynamic interaction leads to large capsule deformation and an irreversible shift in the trajectories of the capsules when they slide over each other with reduced dissipation. Similar irreversible trajectory shifts that increase the initial cross flow separation of the capsules have also been observed for a pair of droplets [19]. This irreversible trajectory shift leads to self-diffusion effects in a suspension of liquid droplets or capsules. Doddi and Bagchi [20] studied the effect of inertia on the hydrodynamic interaction between two spherical capsules in shear flow. Based on their simulations, different types of interaction such as self-diffusive type interaction and spiraling motion are identified at finite inertia. The spiraling motion, in which the capsules reversed their direction of motion progressively in time, is due to the assumption that the flow domain is periodic in the undisturbed flow direction. Finally, it is worth noting that several numerical techniques has been proposed recently [11,21,22] to simulate a large number of three-dimensional deformable particles in order to capture suspension rheology and self-diffusion which are important in many applications. On the other hand, experimentally, Kantsler *et al.* [23] were the first to study the hydrodynamic interaction of two vesicles of similar size and discussed their implications for the rheology of semidilute suspension of vesicles. As in the case of droplets and capsules, deformable vesicles can cross over each other and the interaction is responsible for the large deformation of vesicles at the near-contact position and the irreversible trajectory shift in the cross flow direction.

In this article we investigate numerically the hydrodynamic interaction between two identical elastic capsules for different initial unstressed shapes, namely spherical, oblate spherical, and biconcave, and for a range of the initial positions of the capsules and the dimensionless shear rate. In our numerical study, the viscosity ratio between the internal and surrounding fluid is assumed to match that of red blood cells *in vivo*. An important feature of our numerical method is the inclusion of the capsule membrane bending stiffness [24]. Previous authors have typically neglected the effect of bending moments in order to reduce the computational cost. Here we use a value for the membrane bending stiffness corresponding to that of the healthy red blood cells. So the objective of our present

*ledv@ihpc.a-star.edu.sg
†chiamkh@ihpc.a-star.edu.sg

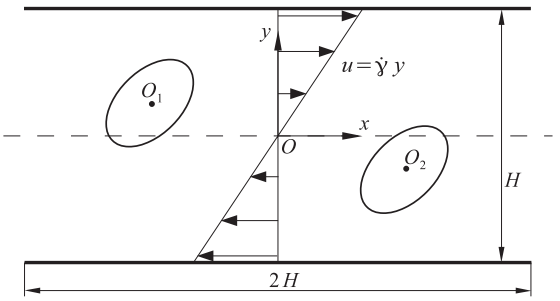

FIG. 1. Initial configuration of a pair of capsules in shear flow. The coordinates of the capsule centered at O_2 are denoted by $(x_0, -y_0)$.

study is to identify different behaviors and types of interaction of capsules in shear flow for a variety of unstressed shapes, considering cases where the viscosity ratio is different from unity, and where the bending stiffness is taken into account.

II. NUMERICAL METHOD

A. Governing equations

In the present study we consider the hydrodynamic interaction between two nonspherical capsules suspended in an ambient fluid with viscosity μ_e, subject to a shear flow as shown in Fig. 1. Each capsule contains a Newtonian fluid with viscosity $\lambda\mu_e$ and is enclosed by a thin shell with undeformed thickness $\bar{h}$. For incompressible fluids, the governing equations are

$$\rho[\boldsymbol{u}_t + (\boldsymbol{u}\cdot\nabla)\boldsymbol{u}] = -\nabla p + \nabla\cdot[\mu(\nabla\boldsymbol{u} + \nabla\boldsymbol{u}^T)] + \boldsymbol{f}, \quad (1)$$

$$\nabla\cdot\boldsymbol{u} = 0, \quad (2)$$

where $\boldsymbol{u} = (u,v,w)^T$ is the fluid velocity, p is the pressure, and ρ and μ are the density and viscosity of the fluid, respectively. The effect of the thin shell $\Omega_S(t)$ immersed in the fluid results in a singular force $\boldsymbol{f}$ which has the form

$$\boldsymbol{f}(\boldsymbol{x},t) = \int_{\Omega_S(t)} \boldsymbol{F}^s(t)\delta[\boldsymbol{x} - \boldsymbol{X}(t)]d\Omega_S, \quad (3)$$

where $\boldsymbol{X}(t)$ is a material point and $\boldsymbol{F}^s(t)$ is the force at time t. Here $\delta(\boldsymbol{x})$ is the three-dimensional Dirac function. The shell follows the local fluid velocity as

$$\frac{d\boldsymbol{X}(t)}{dt} = \int_{\Omega_F} \boldsymbol{u}(\boldsymbol{x},t)\delta[\boldsymbol{x} - \boldsymbol{X}(t)]d\boldsymbol{x}. \quad (4)$$

In describing the kinematics of the capsule membrane, we adopt the thin-shell model [25,26] formulated based on the Kirchhoff-Love hypothesis. Consider a shell body Ω_S whose undeformed and deformed middle surfaces are denoted by $\bar{\Gamma}$ and Γ, respectively. The surface basis vectors corresponding to $\bar{\Gamma}$ and Γ are

$$\bar{\boldsymbol{a}}_\alpha = \bar{\boldsymbol{X}}(\xi^1,\xi^2)_{,\alpha}, \quad \boldsymbol{a}_\alpha = \boldsymbol{X}(\xi^1,\xi^2)_{,\alpha}, \quad (5)$$

respectively, where $\bar{\boldsymbol{X}}$ and $\boldsymbol{X}$ are the positions of a material point associated with the curvilinear coordinates (ξ^1,ξ^2) on the shell middle surface in its undeformed and deformed configurations, respectively. Here and henceforth a comma is used to denote partial differentiation, Greek indices take the values 1 and 2, lowercase Latin indices range from 1 to 3, summation over repeated indices is implied, and a quantity in the undeformed configuration is represented with a bar. The local covariant basis vectors are defined as

$$\boldsymbol{g}_\alpha = \boldsymbol{a}_\alpha + \xi^3(\eta\boldsymbol{a}_3)_{,\alpha}, \quad \boldsymbol{g}_3 = \eta\boldsymbol{a}_3, \quad (6)$$

where ξ^3 is the thickness coordinate, η is the thickness stretch, and $\boldsymbol{a}_3$ is the unit normal vector to the middle surface. The contravariant basis vector $\boldsymbol{g}^i$ is defined such that $\boldsymbol{g}_i\cdot\boldsymbol{g}^j = \delta_i^j$ where δ_i^j is the Kronecker delta. The corresponding covariant and contravariant components of the metric tensors are $g_{ij} = \boldsymbol{g}_i\cdot\boldsymbol{g}_j$ and $g^{ij} = \boldsymbol{g}^i\cdot\boldsymbol{g}^j$, respectively. In term of the co- and contravariant basis vectors, the deformation gradient tensor $\mathbf{F}$ for the shell body may be expressed in the form [27]

$$\mathbf{F} = \frac{\partial\boldsymbol{X}}{\partial\bar{\boldsymbol{X}}} = \frac{\partial\boldsymbol{X}}{\partial\xi^i}\otimes\bar{\boldsymbol{g}}^i = \boldsymbol{g}_i\otimes\bar{\boldsymbol{g}}^i. \quad (7)$$

Using the local covariant basis vectors expressed in Eq. (6), the deformation gradient can be rewritten as

$$\mathbf{F} = \boldsymbol{a}_\alpha\otimes\bar{\boldsymbol{g}}^\alpha + \eta\boldsymbol{a}_3\otimes\bar{\boldsymbol{g}}^3 + \xi^3(\eta\boldsymbol{a}_3)_{,\alpha}\otimes\bar{\boldsymbol{g}}^\alpha. \quad (8)$$

The right Cauchy-Green strain tensor is then given in terms of the deformation gradient tensor $\mathbf{F}$ as

$$\mathbf{C} = \mathbf{F}^{\mathrm{T}}\mathbf{F} = g_{ij}\bar{\boldsymbol{g}}^i\otimes\bar{\boldsymbol{g}}^j. \quad (9)$$

To describe the mechanical response of the thin shell we assign strain-energy functions W, per unit undeformed volume of $\bar{\Omega}$, and H, per unit area of Γ. The total strain energy of the thin shell is defined by

$$\mathrm{S} = \int_{\bar{\Omega}_S} W d\bar{\Omega}_S + \int_\Gamma \mathrm{H} d\Gamma. \quad (10)$$

For the incompressible hyperelastic material, such as Mooney elastic solids or biological membranes, we consider the Mooney-Rivlin strain energy function per unit undeformed volume

$$W(\mathbf{C}) = c_1\big(I_1^C - 3\big) + c_2\big(I_2^C - 3\big), \quad (11)$$

where c_1 and c_2 are material constants and I_1^C and I_2^C are the invariants of the right Cauchy-Green tensor $\mathbf{C}$. The neo-Hookean strain energy function

$$W(\mathbf{C}) = \frac{E}{6}\big(I_1^C - 3\big) \quad (12)$$

is a special case of the Mooney-Rivlin strain energy function with $c_2 = 0$ and $c_1 = E/6$, where E is the Young's modulus. To model the red blood cell membrane, we use the strain energy function proposed by Skalak *et al.* [28]

$$W = \frac{E_s}{4}\left(\frac{1}{2}I_1^2 + I_1 - I_2\right) + \frac{c_{11}E_s}{8}I_2^2, \quad (13)$$

where $E_s = E\bar{h}$ is the surface elastic modulus, c_{11} is a large constant represents the ratio between the area dilatation modulus and the shear modulus, and the invariants I_1 and I_2 are given in [29]. In addition, we consider the Helfrich [30] bending energy function for biological membranes, given by

$$\mathrm{H} = 2\kappa_B\big(\kappa_m - \kappa_m^R\big)^2, \quad (14)$$

where κ_B is the scalar bending modulus and κ_m^R is the reference mean curvature. The mean curvature κ_m is computed from the relation

$$2\kappa_m = \kappa_{\alpha\beta} g^{\alpha\beta}, \tag{15}$$

where $\kappa_{\alpha\beta} = \boldsymbol{a}_{\alpha,\beta} \cdot \boldsymbol{a}_3$ is the component of the curvature tensor.

The Kirchhoff stress tensor can be expressed as

$$\boldsymbol{\tau} = \tau^{ij} \boldsymbol{g}_i \otimes \boldsymbol{g}_j, \tag{16}$$

with the components $\tau^{ij} = 2\frac{\partial W}{\partial g_{ij}} - p_s g^{ij}$, where p_s denotes the hydrostatic pressure. The hydrostatic pressure can be calculated from the plane stress assumption by requiring that $\tau^{33} = 0$. The thickness strain g_{33} and thickness stretch η can be computed from the incompressibility condition $\det \mathbf{F} = 1$. Following [25,26], we define the stress resultant $\boldsymbol{n}^i$ and the moment resultant $\boldsymbol{m}^\alpha$ as

$$\boldsymbol{n}^i = \int_{-\bar{h}/2}^{\bar{h}/2} \boldsymbol{\tau} \cdot \boldsymbol{g}^i \bar{\nu} d\xi^3, \tag{17}$$

$$\boldsymbol{m}^\alpha = \int_{-\bar{h}/2}^{\bar{h}/2} \boldsymbol{\tau} \cdot \boldsymbol{g}^\alpha \xi^3 \bar{\nu} d\xi^3, \tag{18}$$

where $\bar{\nu}$ accounts for the curvature of the shell in the volume integration [29]. The bending stress follows from (14) by the work conjugacy, with the result

$$q^{\alpha\beta} = \frac{\partial \mathrm{H}}{\partial \kappa_{\alpha\beta}} = 2\kappa_B \left(\kappa_m - \kappa_m^R\right) g^{\alpha\beta}. \tag{19}$$

At equilibrium, the potential energy of the shell body is stationary, that is,

$$\delta\Pi = \delta\Pi_{\mathrm{int}} + \delta\Pi_{\mathrm{ext}} = 0, \tag{20}$$

where $\delta\Pi_{\mathrm{ext}}$ is the variation of the potential energy of the external forces. The variation of the potential of the internal forces can be expressed as

$$\delta\Pi_{\mathrm{int}} = \int_{\bar{\Omega}_S} \frac{\partial W}{\partial \mathbf{F}} : \delta\mathbf{F} d\bar{\Omega}_S + \int_\Gamma \frac{\partial \mathrm{H}}{\partial \kappa_{\alpha\beta}} \delta\kappa_{\alpha\beta} d\Gamma. \tag{21}$$

Substituting Eqs. (8) and (19) into (21) and a straightforward manipulation yields the following formulation:

$$\int_{\bar{\Gamma}} [\boldsymbol{n}^\alpha \cdot \delta\boldsymbol{a}_\alpha + \eta\, \boldsymbol{n}^3 \cdot \delta\boldsymbol{a}_3 + \boldsymbol{m}^\alpha \cdot (\eta\delta\boldsymbol{a}_3)_{,\alpha}] d\bar{\Gamma} + \int_\Gamma q^{\alpha\beta} \left(\delta\boldsymbol{a}_{\alpha,\beta} \cdot \boldsymbol{a}_3 + \boldsymbol{a}_{\alpha,\beta} \cdot \delta\boldsymbol{a}_3\right) d\Gamma + \delta\Pi_{\mathrm{ext}} = 0. \tag{22}$$

Details for the derivation of Eq. (22) are given in [25,29].

B. Spatial discretization of the thin shell

Here we follow the C^1-interpolation scheme based on the subdivision surface proposed in [25,31] for thin-shell analysis. The main idea behind subdivision surfaces is to represent the smooth shell middle surface by a control mesh containing a set of NP control points $\mathbf{x}_I, I = 1, \ldots, \mathrm{NP}$. This mesh may be taken as a basis for introducing an interpolation of the form

$$\mathbf{x}(\xi^1,\xi^2) = \sum_I N^I(\xi^1,\xi^2)\mathbf{x}_I, \tag{23}$$

where I is the local numbering of the nodes and $N^I(\xi^1,\xi^2)$ is the box-spline basis function [32]. Introducing the interpolated parametric equation (23) into the weak form (22), we arrive at the formulation for the internal force at node I as

$$\boldsymbol{f}_I = \int_{\bar{\Gamma}} \left[\boldsymbol{n}^\alpha \cdot \frac{\partial \boldsymbol{a}_\alpha}{\partial \mathbf{x}_I} + \eta \boldsymbol{n}^3 \cdot \frac{\partial \boldsymbol{a}_3}{\partial \mathbf{x}_I} + \boldsymbol{m}^\alpha \cdot \left(\eta \frac{\partial \boldsymbol{a}_3}{\partial \mathbf{x}_I}\right)_{,\alpha}\right] d\bar{\Gamma} + \int_\Gamma q^{\alpha\beta} \left[\left(\frac{\partial \boldsymbol{a}_\alpha}{\partial \mathbf{x}_I}\right)_{,\beta} \cdot \boldsymbol{a}_3 + \boldsymbol{a}_{\alpha,\beta} \cdot \frac{\partial \boldsymbol{a}_3}{\partial \mathbf{x}_I}\right] d\Gamma. \tag{24}$$

The internal force at node I is the sum of element contributions as in the standard finite element method. The contribution to the internal force at node I from a generic element can be calculated by a one-point quadrature rule [25] with the barycenter of the element as the Gaussian quadrature point. The stress and moment resultants at the quadrature point are computed by numerical integration of the stresses across the thickness of the shell using the three-point Simpson rule.

C. Description of the immersed boundary method

The coupling between the fluid and the capsule deformation is done using an implicit immersed boundary method [29] which is an extension of Peskin's immersed boundary method [33]. In this method, the force density is computed at the control points and is distributed to the Cartesian grid points using a discrete δ function,

$$\boldsymbol{f}(\boldsymbol{x},t) = \sum_{I=1}^{\mathrm{NP}} \boldsymbol{f}_I(\xi^1,\xi^2,t) D_h[\boldsymbol{x} - \mathbf{x}_I(t)] \triangle\xi^1 \triangle\xi^2, \tag{25}$$

where $\boldsymbol{f}_I(\xi^1,\xi^2,t)$ is the force per unit area at the control point $\mathbf{x}_I$ whose label is (ξ^1,ξ^2) and $D_h(\boldsymbol{x})$ is a three-dimensional discrete δ function [34]. Once the force density is computed at the control points and distributed to the grid, the Navier-Stokes equations with the forcing terms are then solved for the pressure and velocity field at the Cartesian grid points using the projection method [35]. The velocity field is then interpolated to find the velocity at the control points as

$$\boldsymbol{u}(\mathbf{x}_I,t) = \sum_{\boldsymbol{x}} \boldsymbol{u}(\boldsymbol{x},t) D_h[\boldsymbol{x} - \mathbf{x}_I(t)] h^3, \tag{26}$$

and this velocity is used to advance the position of the immersed boundary in an implicit manner [29]. The method used in the present study has been tested extensively for the deformation of single elastic capsule in shear flow in our previous work [24,31].

III. RESULTS

In this section we investigate the hydrodynamic interaction of two identical capsules enclosed by thin shells with spherical, spheroidal, and biconcave unstressed shapes in simple shear flow given by the velocity $\boldsymbol{u} = (\dot{\gamma} y, 0, 0)$, where $\dot{\gamma}$ is the shear rate. Nondimensionalizing all variables using as length scale the equivalent volumetric capsule radius a, time scale the inverse shear rate $\dot{\gamma}^{-1}$, and stress $\dot{\gamma}\mu_e$, we find that the deformation and interaction of the capsules are determined by five parameters: the Reynolds number $Re = \rho\dot{\gamma}a^2/\mu_e$, the dimensionless shear rate $G = \mu_e\dot{\gamma}a/(E\bar{h})$, the reduced ratio of the bending modulus to the elastic modulus $\hat{\kappa}_B = \kappa_B/(a^2 E\bar{h})$,

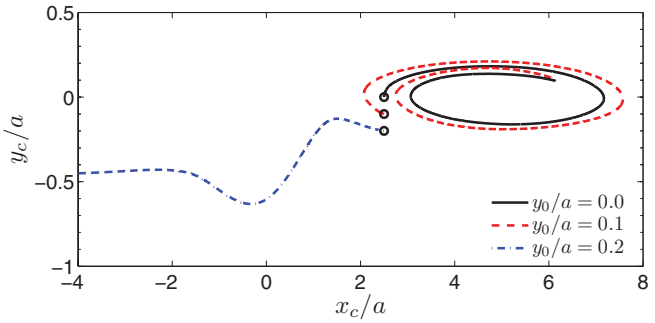

FIG. 2. (Color online) Trajectories of the spherical capsule center O_2 with $G = 0.2$ and $x_0/a = 2.5$ at different initial locations $y_0/a = 0, 0.1, 0.2$. The circle symbols are the initial locations $(x_0, -y_0)$ of the capsule center O_2.

the viscosity ratio λ, and the relative initial position of the capsules. For a capsule of volume V, the equivalent volumetric radius $a = (3V/4\pi)^{1/3}$ is chosen to be sufficiently small so that the inertia effect can be neglected ($Re \ll 1$). Therefore, the deformation and interaction of the capsules only depend on the last four parameters, namely, dimensionless shear rate G, reduced bending modulus $\hat{\kappa}_B$, viscosity ratio λ, and the relative initial position of the capsules. The healthy red blood cell membrane's elastic modulus $E\bar{h}$ and bending modulus κ_B are on the order of 10^{-3} dyn/cm and 10^{-12} dyn/cm, respectively [36]. Taking the volume of a red blood cell to be $V \approx 7 \times 10^{-11}$ cm^3, the reduced bending modulus $\hat{\kappa}_B$ is then on the order of 10^{-2}. The ratio of the viscosity of the red blood cell interior fluid to the viscosity of the suspending fluid *in vivo* ranges between 4 and 10. Hence, all the simulations are performed for a fixed bending modulus $\hat{\kappa}_B = 0.01$ and viscosity ratio $\lambda = 4$ with different initial positions and dimensionless shear rates G. We have kept Re fixed at $Re = 0.01$. Experimentally, it is most convenient to vary G by varying the shear rate $\dot{\gamma}$. Thus, in practice, varying G results in Re varying too. However, at the low values of Reynolds numbers encountered in this study, inertia effects are negligible and Re is not expected to affect the capsule dynamics. Indeed, it has previously been shown that capsule

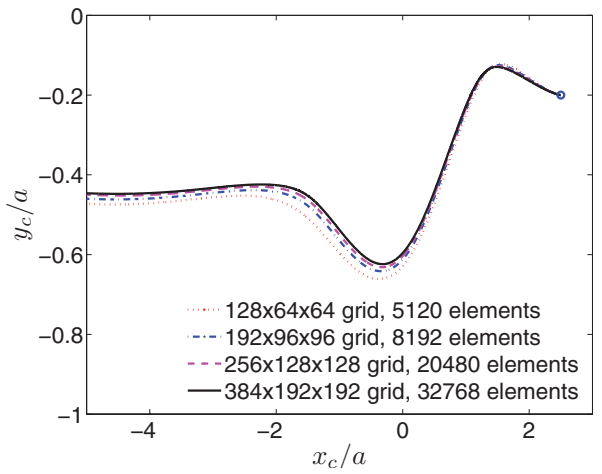

FIG. 3. (Color online) Grid refinement study on the trajectories of the spherical capsules when they cross over each other.

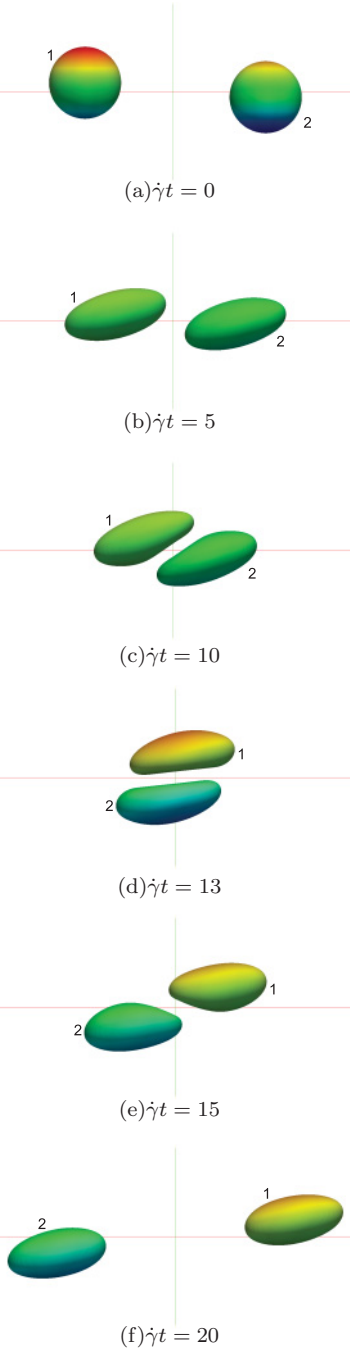

FIG. 4. (Color online) Snapshots of capsules during a self-diffusive type or crossing interaction, corresponding to the case of $y_0/a = 0.2$ in Fig. 2.

deformation, as measured by the Taylor shape parameter $D_{xy} = (L - B)/(L + B)$, where L and B are the maximum and minimum radial distances of an ellipsoid with the same inertia tensor [8], as well as the capsule inclination angle, are independent of Re when $Re < 0.1$ [29]. Extensive simulations over a wide range of Re have also been carried out by Doddi and Bagchi [20]. They showed that the effect of inertia is not important when $Re < 0.5$. Therefore, in this study, we have varied G and kept Re constant.

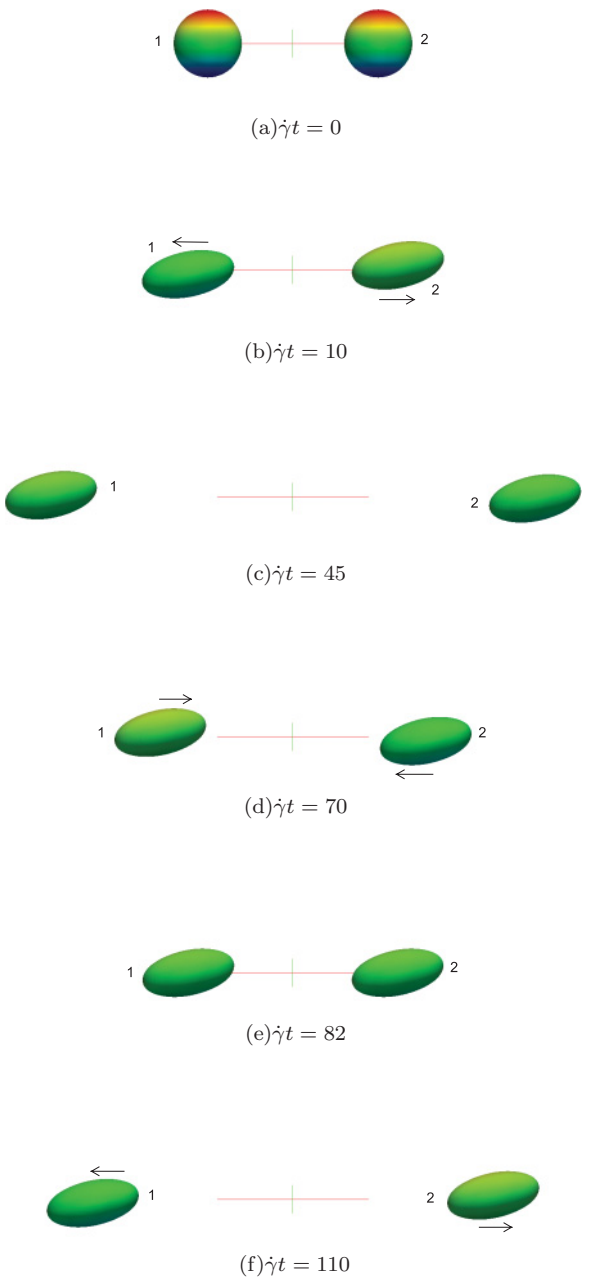

FIG. 5. (Color online) Snapshots of capsules during a spiraling motion, corresponding to the case of $y_0/a = 0$ in Fig. 2.

The deformation of the capsules is described by the Taylor shape parameter defined above. Simulations are performed on a computational domain of size $20a \times 10a \times 10a$ discretized with a $256 \times 128 \times 128$ fluid grid with Dirichlet boundary condition for the velocity at $y = \pm 5a$ and periodic at other boundaries. We use an unstructured surface mesh of 10 242 nodes and 20 480 elements to represent the capsule surface and the initial capsule shape is taken to be a reference state for both in-plane tensions and bending moments. These fluid grid and surface mesh are fine enough to capture the interaction of the two capsules. In some calculations we perform grid refinement study to further confirm the independence of grid sizes on the interaction of the capsules.

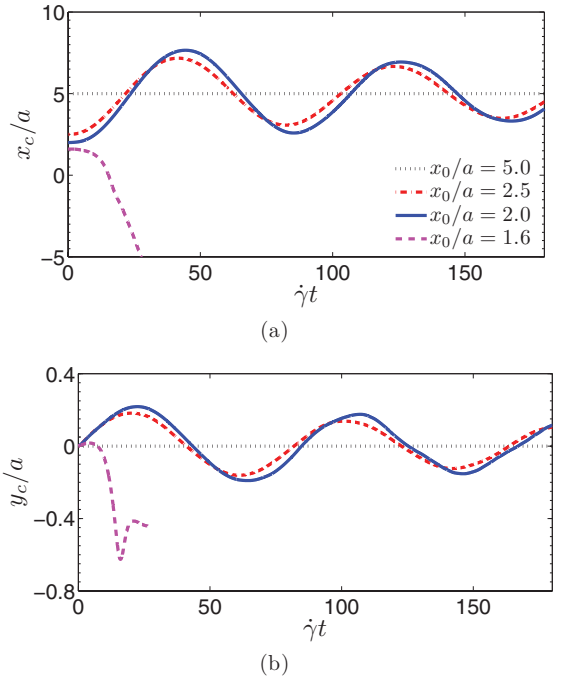

FIG. 6. (Color online) Location of the spherical capsule center O_2, (x_c, y_c) for $y_0/a = 0$ and various values of x_0/a, and with $G = 0.2$: (a) x_c/a vs dimensionless time $\dot{\gamma}t$, (b) y_c/a vs $\dot{\gamma}t$. Snapshots for the case of $x_0/a = 2.5$ are depicted in Fig. 5.

A. Spherical capsules

First we investigate the hydrodynamic interaction between two neo-Hookean spherical capsules with their centers of mass O_1 and O_2 initially located in the same shear plane at $(-x_0, y_0, 0)$ and $(x_0, -y_0, 0)$, respectively. Figure 2 shows the trajectories of the capsule center of mass O_2, $(x_c, y_c, 0)$, for different initial locations $y_0/a = 0$, 0.1, 0.2. Here we consider $G = 0.2$ and $x_0/a = 2.5$. At $y_0/a = 0.2$, the capsules approach and interact with each other and result in an irreversible shift in their trajectories. To confirm that the capsules behavior does not depend on the meshes, grid refinement study is carried out for four different fluid grids, that is, $128 \times 64 \times 64$, $192 \times 96 \times 96$, $256 \times 128 \times 128$, and $384 \times 192 \times 192$ grids with the corresponding surface meshes of 5120, 8192, 20 480 and 32 768 triangular elements, respectively. Figure 3 shows the general trend toward convergence of the trajectories of the capsules. Snapshots of capsules during the interaction are shown in Fig. 4. As the capsules approach each other, the vertical separation distance between them decreases first and increases when they cross over each other. Then the vertical separation decreases and maintains a constant value as they move away from each other until they reach the end of the computational domain. This type of interaction has also been observed in [17,20] and is referred to as a self-diffusive type interaction.

When the initial vertical coordinate is $y_0/a = 0.1$, the capsules approach each other due to the nonzero relative velocity between them. However, they do not cross over each other upon encounter, as was the case of $y_0/a = 0.2$. Instead, they reverse their directions of motion when their centers of mass cross the $y = 0$ axis as seen in Fig. 2. After the reversal

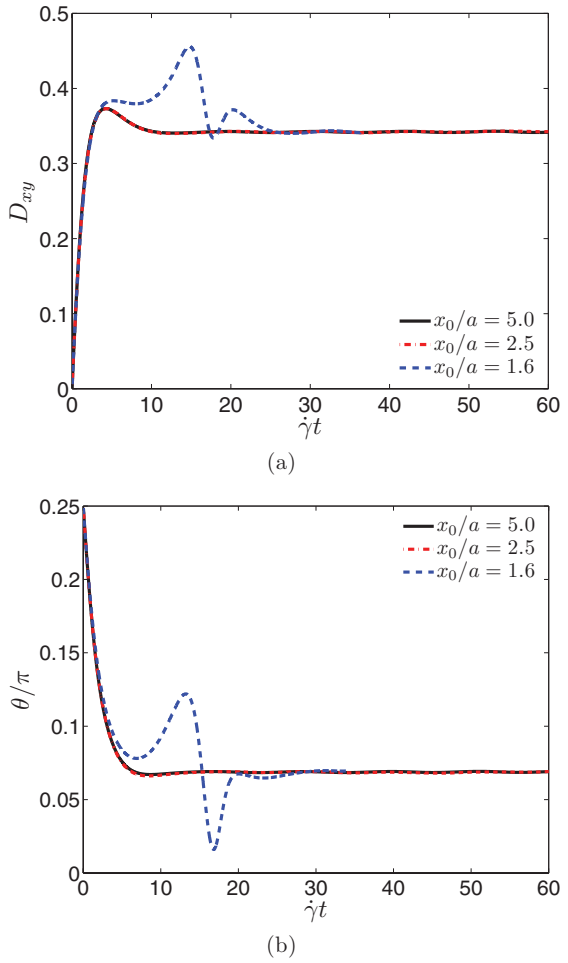

FIG. 7. (Color online) Temporal evolution of (a) the deformation parameter D_{xy} and (b) the inclination angle θ/π for a spherical capsule with $G = 0.2$ at $y_0/a = 0$ and various x_0/a. Snapshots for the case of $x_0/a = 2.5$ are depicted in Fig. 5.

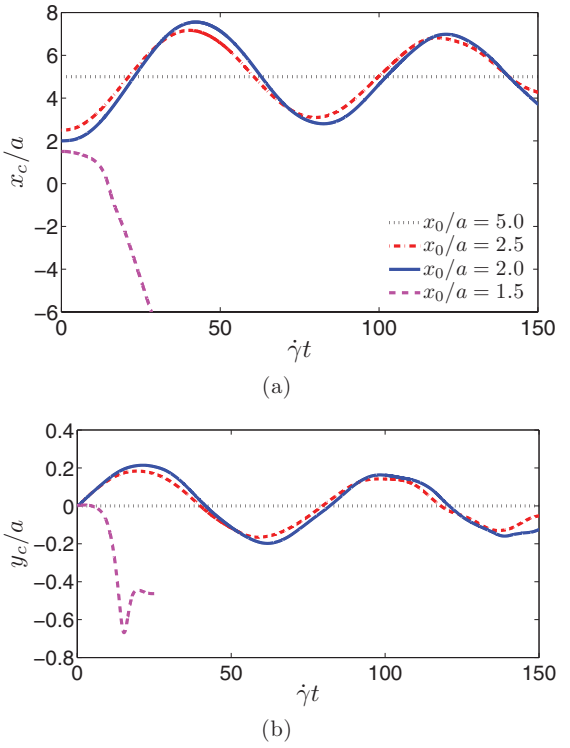

FIG. 8. (Color online) Location of the oblate spheroidal capsule with aspect ratio $k = 0.9$ and center O_2 for $y_0/a = 0$ and various values of x_0/a, and with $G = 0.1$: (a) x_c/a vs $\dot{\gamma}t$, (b) y_c/a vs $\dot{\gamma}t$.

of direction, the capsules move away from each other and subsequently reverse their directions of motion again when they "see" each other again at the end of the computational domain due to the periodic boundary condition. Similar motion has been observed in [37] between two two-dimensional elastic particles at Reynolds number $Re = 0.1$. Doddi and Bagchi [20] also observed similar spiraling motion of the capsules when they took into account the effects of inertia.

For $y_0/a = 0$ we observe the same reversal motion as the previous case. However the capsules do not approach each other initially because there is no relative center velocity imposed by the undisturbed flow. They start to move in the opposite directions right at the beginning of the simulation. Figure 5 shows such a sequence of capsule-capsule interactions. This is quite different from what was observed in [20], which showed no interaction between the capsules in the limit $y_0/a \to 0$. However, Lac *et al.* [17] observed the crossing of the two capsules even when there is no *a priori* relative center velocity, that is, $y_0/a = 0$. This is because the tank-treading motion of the capsule membrane creates a three-dimensional disturbance flow which tends to move the capsule centers off the x axis and leads to the crossing. We believe that this is also the reason for the spiraling motion observed in our simulation with $y_0/a = 0$. In addition, the capsules are not initially placed symmetrically in the periodic domain and the flow will force the capsules to oscillate before moving to an equilibrium position. If the capsules are located symmetrically in the periodic domain, that is, $x_0/a = 5$, they will deform to a steady shape and exhibit tank-treading motion at their initial locations without oscillating. This can be seen clearly in Fig. 6 in which the x and y coordinates of the capsule center O_2 are shown for several values of x_0 along with $y_0/a = 0$.

When the capsules are located symmetrically in the periodic domain, that is, $x_0/a = 5$ and $y_0/a = 0$, the capsule center components x_c and y_c will remain constant with time. In this case, there is no interaction between the capsules and each capsule exhibits the same motion as for the case of single capsule in shear flow. However, for $x_0/a = 2.5$ or $x_0/a = 2$, the capsules exhibit the damped oscillations in both x_c and y_c as can be seen in Fig. 6 and eventually converge to the equilibrium position $x_0/a = 5$. This type of motion is referred to as spiraling motion [20]. When the capsules are placed closer to each other, that is, $x_0/a = 1.6$, they start to interact even before they reach a steady deformed state and subsequently they roll over each other. And the capsule on the right continues to move to the left to the end of the computational domain as shown in Fig. 6(a). Figure 7 shows the evolution of deformation parameter and inclination angle during capsule-capsule interaction. During the capsule spiraling motion the deformation parameter and inclination angle reach the steady states which are the same as those at equilibrium position. But when the capsules cross over each other the deformation parameter and inclination angle

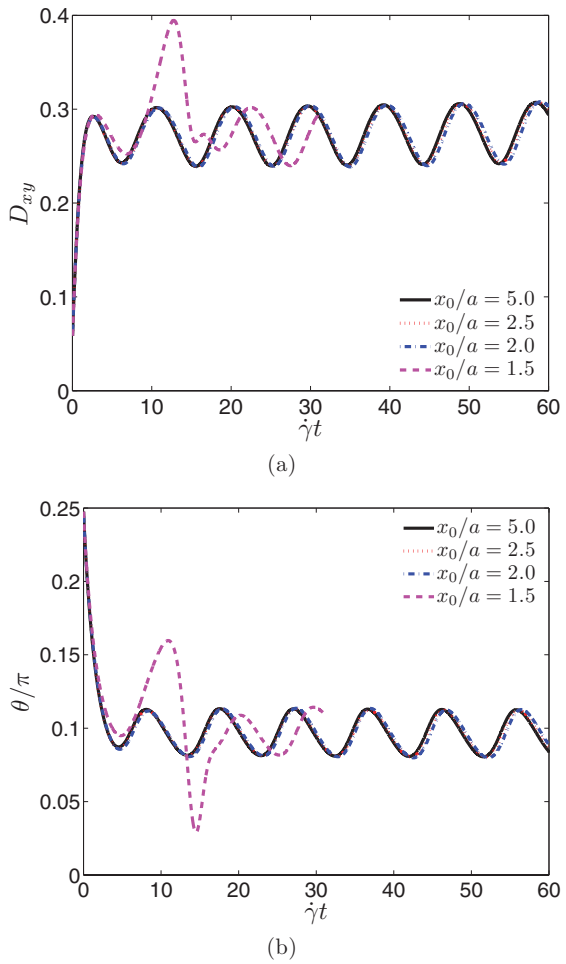

FIG. 9. (Color online) Temporal evolution of (a) the deformation parameter D_{xy} and (b) the inclination angle θ/π for the oblate spheroidal capsule with $k = 0.9$ and $G = 0.1$ at $y_0/a = 0$ and various x_0/a.

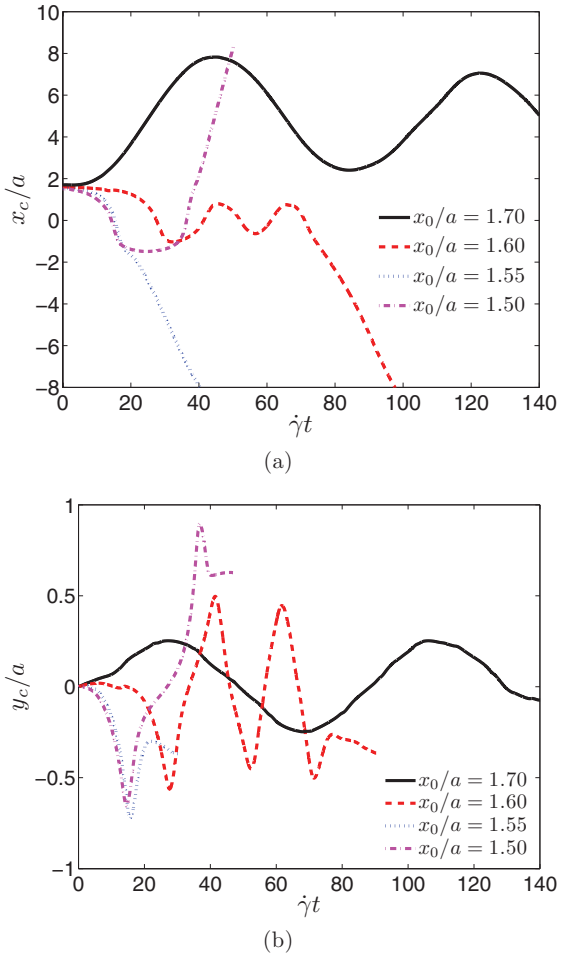

FIG. 10. (Color online) Location of the oblate spheroidal capsule with aspect ratio $k = 0.3$ and center O_2 for $y_0/a = 0$ and various values of x_0/a, and with $G = 0.05$: (a) x_c/a vs $\dot{\gamma}t$, (b) y_c/a vs $\dot{\gamma}t$.

change substantially before reaching the equilibrium values as they separate. We can also see the angular deviation from the stationary inclination angle during the crossing.

B. Oblate spheroidal capsules

Next we consider the interaction of two neo-Hookean capsules with oblate spheroidal unstressed shapes. An oblate spheroid with aspect ratio of k is described by the mapping $x_{\rm obl} = Rx, y_{\rm obl} = Ry, z_{\rm obl} = kRz$, where (x,y,z) is the coordinate of a point on the unit sphere and the radius R is adjusted to preserve the capsule volume. The capsules are inclined at an angle $\theta_0 = \pi/4$ with respect to the streamlines of the undisturbed flow. Figure 8 shows the time evolution of the centers of the oblate spheroid capsules with aspect ratio $k = 0.9$ at dimensionless shear rate $G = 0.1$. In these simulations, the capsules are initially located at $y_0/a = 0$ and their horizontal separations x_0/a are varied. Since the oblate spheroids with $k = 0.9$ are nearly spherical capsules, their trajectories tend to be similar to those of the spherical capsules shown in Fig. 6. The capsule center components x_c and y_c remain constant with time at $x_0/a = 5$ while their values oscillate for $x_0/a = 2.5$ and $x_0/a = 2$ in a spiraling manner. And when the capsules initially placed closer to each other at $x_0/a = 1.5$ we will see the crossing of the two capsules.

Figure 9 shows the evolution of the deformation parameter and the inclination angle of the capsules for different initial locations. It can be seen that the capsules undergo periodic oscillations in both deformation parameter and inclination angle superimposed on the tank-treading motion, which is commonly referred to as swinging motion [4]. The frequency

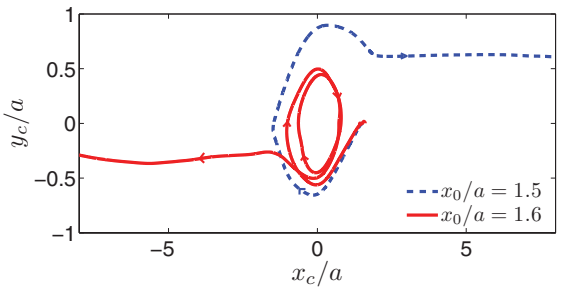

FIG. 11. (Color online) Trajectories of the capsule center O_2 with $k = 0.3$, $G = 0.05$, and initial positions $x_0/a = 1.5$ and 1.6, and $y_0/a = 0$. The blue dashed curve illustrates the swapping motion as discussed in the text.

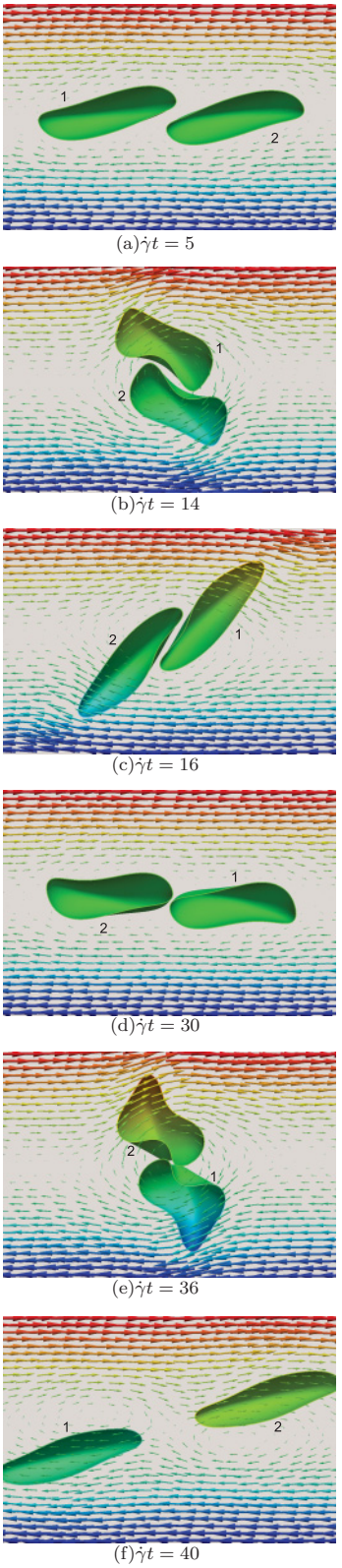

FIG. 12. (Color online) Snapshots of oblate spheroidal capsules with $k = 0.3$ and $G = 0.05$ and fluid velocity field (background arrows) in the (x, y) plane illustrating a swapping motion. The initial location of the capsule is $x_c/a = 1.5$, $y_c/a = 0$.

and the amplitude of the oscillations in the deformation parameter and inclination angle are exactly the same as when

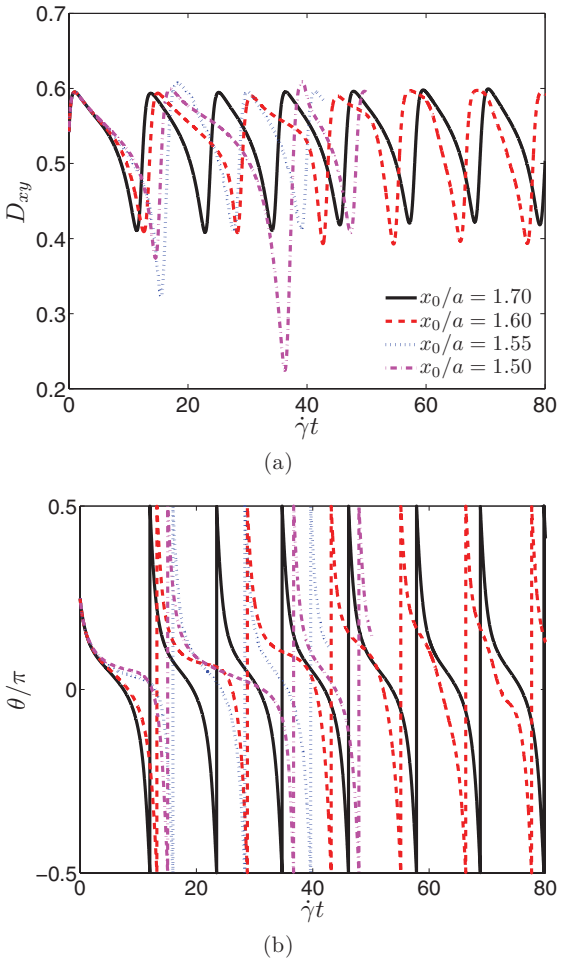

FIG. 13. (Color online) Temporal evolution of (a) the deformation parameter D_{xy} and (b) the inclination angle θ/π for an oblate spheroidal capsule with $k = 0.3$ and $G = 0.05$ at different x_0/a and $y_0/a = 0$.

two capsules undergo spiraling motion ($x_0/a = 2, 2.5$) or when there is no interaction between capsules ($x_0/a = 5$). However, when the capsules cross each other ($x_0/a = 1.5$), there are significant differences in both deformation parameter and inclination angle. This is because, during the crossing, both capsules are elongated and the inclination angle changes rapidly before return to normal when the capsules separate.

We then consider the interaction of two oblate spheroid capsules of aspect ratio $k = 0.3$, inclined at the angle $\theta_0 = \pi/4$ with respect to the streamlines of the unperturbed flow. This more oblate unstressed shape of aspect ratio $k = 0.3$ is chosen because of its comparable sphericity [8] with the red blood cell considered in the next section. The trajectory, deformation parameter, and inclination angle are calculated for $G = 0.05$, at initial positions $y_0/a = 0$ with different values of x_0/a. Figure 10 shows different trajectories of the capsule O_2 with $x_0/a = 1.7$, 1.6, 1.55, and 1.5. Despite the small variation in the horizontal separation, the capsules exhibit different types of interaction. When the capsules are located far enough, that is, $x_0/a = 1.7$, they will approach and reverse their direction of motion upon encounter in a spiraling manner as observed previously. For $x_0/a = 1.55$, the capsules approach and roll over each other and eventually separate in the x direction.

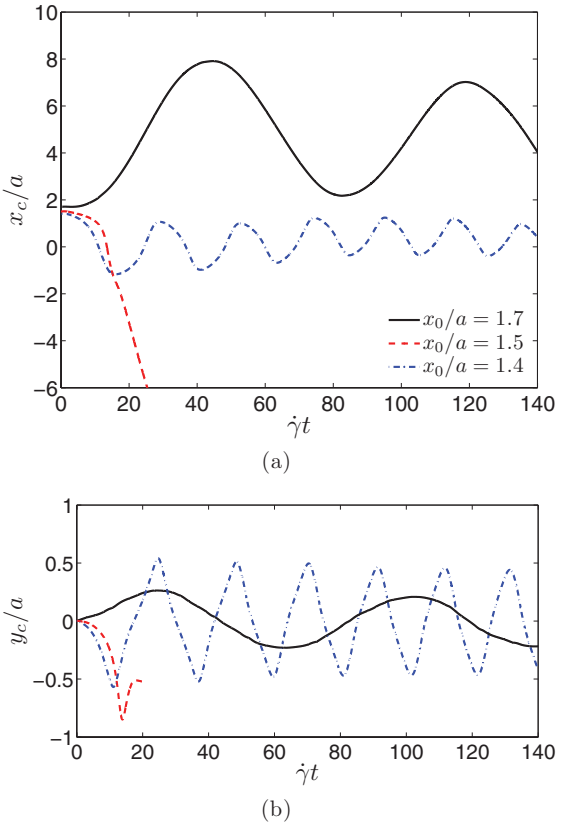

FIG. 14. (Color online) Location of the biconcave capsule center O_2, (x_c, y_c) for $y_0/a = 0$ and various values of x_0/a, and with $G = 0.1$: (a) x_c/a vs $\dot{\gamma}t$, (b) y_c/a vs $\dot{\gamma}t$.

For the other two initial locations, we see a new behavior of the capsules before they separate. At $x_0/a = 1.6$, the capsules rotate around each other two and a half times before separating. At $x_0/a = 1.5$, the capsules rotate around each other for just one time before crossing. This motion is similar to the swapping motion observed in [38] for two rigid spheres in shear flow in a wall-bounded system. This can be seen clearly in Fig. 11 where the trajectories of the capsule center O_2 are shown for $x_0/a = 1.6$ and 1.5. It is worth noting that the final lateral shift for the case of initial location $x_0/a = 1.5$ is much larger than that when $x_0/a = 1.6$. This implies that the interaction of the capsules before separation also affects the final lateral displacement between capsules, not just the initial vertical separation or Reynolds number [20]. Figure 12 shows the snapshots of the capsules with initial location $x_0/a = 1.5$ as they rotate around each other. In Fig. 12(a) the capsules approach and slide over each other and gradually enter the vortex zone as shown in Fig. 12(b). The capsules then rotate around each other which can be seen in Figs. 12(c)–12(e). When the capsules reach their highest positions [Figs. 12(e) and 10(b)], the shear flow is strong enough to separate them and eventually results in a permanent separation as shown in Fig. 12(f).

Finally, in Fig. 13, we show the evolution of the deformation parameter and the inclination angle of the oblate spheroidal capsules. The capsules exhibit tumbling motion in which the capsules undergo continuous rotation as shown in Fig. 13(b). When the capsules show the spiraling motion, the deformation

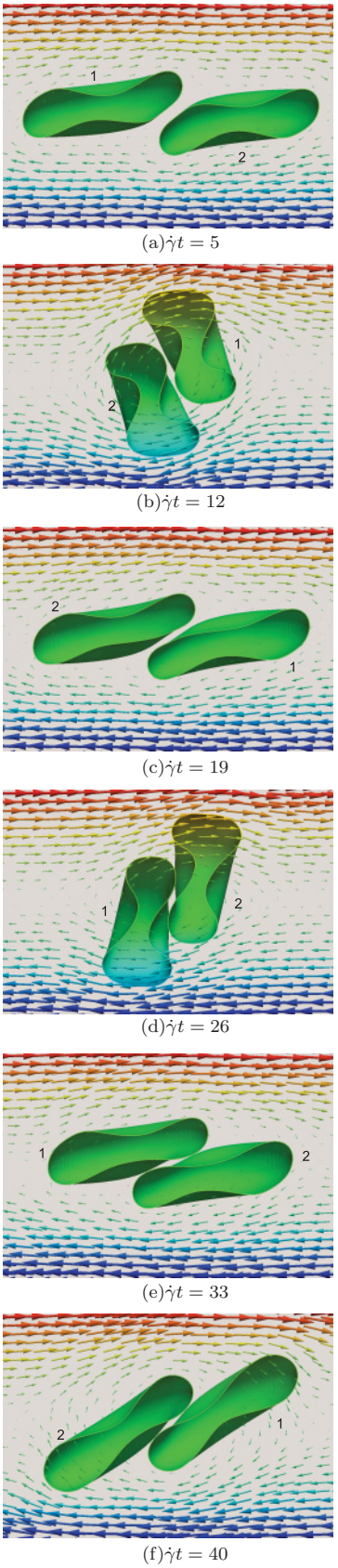

FIG. 15. (Color online) Snapshots of biconcave capsules with $G = 0.1$ and fluid velocity field (background arrows) in the (x, y) plane illustrating continuous rotating motion. The initial location of the capsule center is $x_0/a = 1.4$, $y_0/a = 0$.

parameter deviates slightly from it initial shape. But when the capsules cross over or rotate around each other (i.e., swapping), we may see large distortion and compression as shown explicitly in Fig. 12(e).

C. Biconcave capsules

Next, we perform simulations for the biconcave capsules with Skalak's strain energy function (13) for red blood cell membrane. In this energy function, the area dilatation modulus c_{11} is chosen to be 50, which is large enough to maintain the constant surface area of the biconcave capsules. The mapping for the biconcave disk shape assumed by red blood cells at rest is given in [29]. The capsules are initially inclined at an angle $\theta_0 = \pi/4$ with respect to the streamlines of the undisturbed flow. The trajectories of biconcave capsules are studied for $G = 0.1$, $y_0/a = 0$ with three different values of x_0/a. Figure 14 shows the time history of x and y components of the capsule center O_2 with the initial location $x_0/a = 1.7$, 1.5,, and 1.4. Since the biconcave capsules have comparable sphericity with the oblate spheroidal capsules of aspect ratio $k = 0.3$, their behaviors during interaction are expected to be similar to those of the oblate spheroidal capsules of $k = 0.3$ as discussed in the previous section. It can be observed that the capsules exhibit the spiraling motion with $x_0/a = 1.7$, but they cross each other when the initial location is $x_0/a = 1.5$. If the capsules are located closer initially at $x_0/a = 1.4$, then they will rotate around each other. However, unlike the oblate spheroidal capsules of $k = 0.3$, the biconcave capsules do not separate but keep rotating around each other during the course of simulation. Figure 15 shows the fluid velocity field in the (x, y) plane and the snapshots of the biconcave capsules with initial location $x_0/a = 1.4$ and $y_0/a = 0$ as they rotate around each other. It can be seen that both capsules are trapped totally within the recirculation zone in the middle of the domain and the outer flow could not separate them. The two capsules behave like one big capsule undergoing tumbling motion. Figure 16 shows the temporal evolution of the inclination angle of the triaxial ellipsoid with the same inertia tensor as that of the two biconcave capsules. We have refined the fluid mesh and surface mesh to show that the rotating behavior of the two

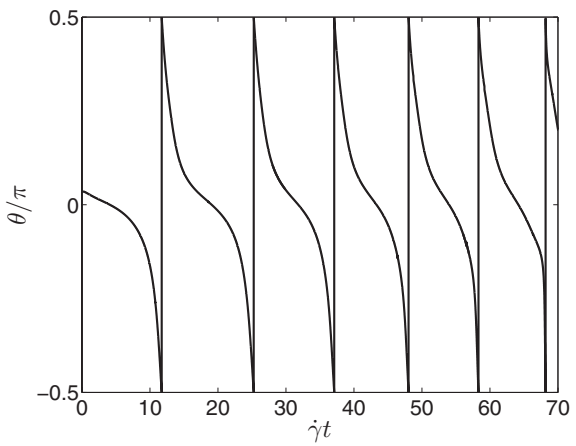

FIG. 16. Inclination angle of an ellipsoid that has the same inertia tensor as that of the two biconcave capsules.

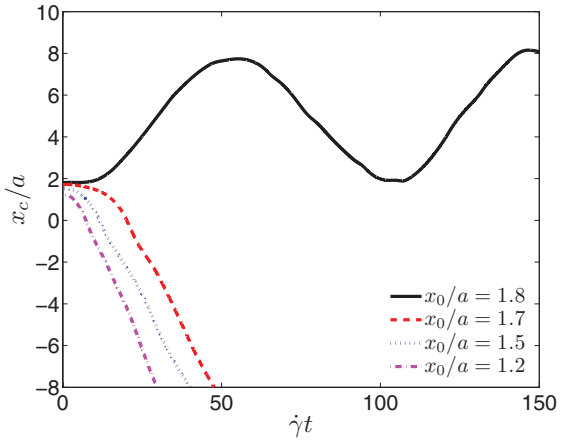

FIG. 17. (Color online) Location of the x component of the biconcave capsule center O_2, x_c, for $y_0/a = 0$ and various values of x_0/a, and with $G = 0.5$.

capsules does not depend on the mesh sizes. Simulations are performed on $384 \times 192 \times 192$ with the surface mesh of 32 768 elements and the two capsules rotate around each other as observed with coarser meshes. While rotating around each other, the capsules undergo tumbling motion. If we increase the dimensionless shear rate G up to the point where the single capsule exhibits swinging motion, the two capsules will not show the relative rotating motion. Figure 17 shows the x component of the capsule center O_2 for $y_0/a = 0$ with different values of x_0/a and for an increased $G = 0.5$. At this higher value of dimensionless shear rate, the capsules undergo swinging motion and they either oscillate in the spiraling motion or cross each other. The capsules do not rotate around each other as observed previously with small dimensionless shear rate. This implies that the individual motion of each capsule such as tumbling or swinging affects the interaction between the two capsules. And whether the capsules exhibit tumbling or swinging motion depends on the dimensionless shear rate and the reduced bending modulus of the capsule membranes.

We now focus on the effect of the initial vertical separation distance between the two capsules on the type of interaction. Simulations are performed for biconcave capsules with $G = 0.1$ at initial location $x_0/a = 5$ and various y_0/a. The center trajectories depend on the initial cross flow separation as shown in Fig. 18 for $y_0/a = 0.2$, 0.3, 0.4,, and 0.5. At $y_0/a \leqslant 0.2$, the capsules reverse their motion progressively

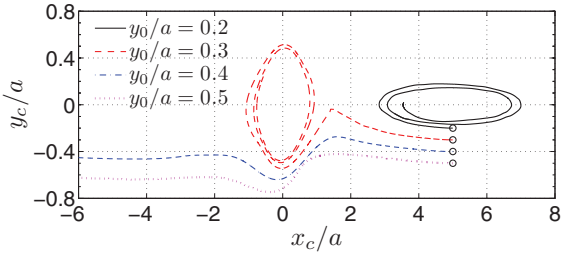

FIG. 18. (Color online) Trajectories of the capsule center O_2 with $G = 0.1$ and different initial positions.

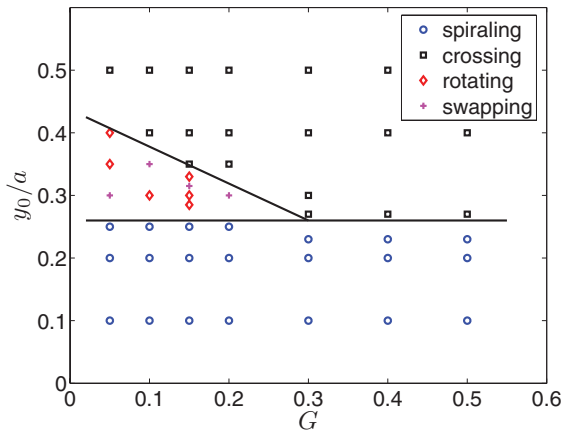

FIG. 19. (Color online) Different types of hydrodynamic interaction between two biconcave capsules at various dimensionless shear rates and initial vertical separation distances. Representative snapshots of these four types of interactions have been shown previously, namely, spiraling in Fig. 5, crossing in Fig. 4, rotating in Fig. 15, and swapping in Fig. 12.

in time while they cross over each other at larger y_0/a, that is, $y_0/a = 0.4$ and 0.5. At moderate initial vertical separation distance $y_0/a = 0.3$, the capsules wrap around each other continuously. Finally, the effects of the initial vertical separation distance and the dimensionless shear rate on the interaction of two biconcave capsules can be summarized in a phase diagram as shown in Fig. 19. At small initial vertical separation distance, that is, $y_0/a \leqslant 0.25$, the two capsules only exhibit spiraling-type interaction where they oscillate around an equilibrium position. At larger initial vertical separation distance, the two capsules cross over each other. However, at low dimensionless shear rates where the capsules undergo tumbling motion, two other types of motion are observed: the capsules rotate around each other or they swap their trajectories. Representative snapshots of these four types of interactions have been shown previously, namely, crossing in Fig. 4, spiraling in Fig. 5, swapping in Fig. 12, and rotating in Fig. 15. We note that we cannot conclusively determine the exact phase boundaries of the rotating and swapping motions. There could be two plausible reasons for this. First, the type of motion observed could depend very sensitively on the initial separation. Therefore, in the future, we plan to develop better numerical methods so that our simulations can be repeated at finer spatial resolutions to probe this sensitive dependence on initial separation. Second, the type of motion observed could be transient and our simulations may not have reached steady state. This can be resolved in future by conducting simulations for longer run times.

IV. CONCLUSIONS

In the article we have studied numerically the hydrodynamic interaction between two nonspherical capsules enclosed by thin shells in shear flow. Several unstressed shapes of the capsules have been considered such as oblate spheroidal and biconcave capsules with neo-Hookean and Skalak strain energy functions. Two types of interaction observed for spherical capsules are crossing (e.g., Fig. 4) and spiraling (e.g., Fig. 5) which depends on the initial separation distances of the capsules in different directions. As the sphericity or aspect ratio of the unstressed shape decreases, we observe the two new interaction types which are swapping motion (e.g., Fig. 12) and continuous rotation (e.g., Fig. 15), in addition to crossing and spiraling. The swapping motion and continuous rotation only occur when the individual capsule undergo tumbling motion at small dimensionless shear rate. In this study we show the effect of the unstressed shape, the dimensionless shear rate, and the initial location of the capsules on the hydrodynamic interaction. We do not investigate the effects of viscosity ratio and bending stiffness, but it would be interesting to carry out parametric study on these parameters since they affect significantly the dynamics of individual capsules and thus the hydrodynamic interaction between the two capsules.

[1] K. Chang and W. Olbricht, J. Fluid Mech. **250**, 609 (1993).
[2] A. Walter, H. Rehage, and H. Leonhard, Colloid Polym. Sci. **278**, 169 (2000).
[3] T. M. Fischer, Biophys. J. **86**, 3304 (2004).
[4] M. Abkarian, M. Faivre, and A. Viallat, Phys. Rev. Lett. **98**, 188302 (2007).
[5] D. Barthès-Biesel and J. Rallison, J. Fluid Mech. **113**, 251 (1981).
[6] J. M. Skotheim and T. W. Secomb, Phys. Rev. Lett. **98**, 078301 (2007).
[7] H. Noguchi, Phys. Rev. E **80**, 021902 (2009).
[8] S. Ramanujan and C. Pozrikidis, J. Fluid Mech. **361**, 117 (1998).
[9] H. Noguchi and G. Gompper, Phys. Rev. Lett. **98**, 128103 (2007).
[10] Y. Sui, Y. T. Chew, P. Roy, X. B. Chen, and H. T. Low, Phys. Rev. E **75**, 066301 (2007).
[11] S. K. Doddi and P. Bagchi, Phys. Rev. E **79**, 046318 (2009).
[12] P. Bagchi and R. M. Kalluri, Phys. Rev. E **80**, 016307 (2009).
[13] C. Misbah, Phys. Rev. Lett. **96**, 028104 (2006).
[14] M. Abkarian and A. Viallat, Soft Matter **4**, 653 (2008).
[15] J. Deschamps, V. Kantsler, and V. Steinberg, Phys. Rev. Lett. **102**, 118105 (2009).
[16] G. Breyiannis and C. Pozrikidis, Theor. Comput. Fluid Dyn. **13**, 327 (2001).
[17] E. Lac, A. Morel, and D. Barthès-Biesel, J. Fluid Mech. **573**, 149 (2007).
[18] E. Lac and D. Barthès-Biesel, Phys. Fluids **20**, 040801 (2008).
[19] M. Loewenberg and E. J. Hinch, J. Fluid Mech. **338**, 299 (1997).
[20] S. Doddi and P. Bagchi, Int. J. Multiphase Flow **34**, 375 (2008).
[21] M. M. Dupin, I. Halliday, C. M. Care, L. Alboul, and L. L. Munn, Phys. Rev. E **75**, 066707 (2007).
[22] R. MacMeccan, J. Clausen, G. Neitzel, and C. Aidun, J. Fluid Mech. **618**, 13 (2009).
[23] V. Kantsler, E. Segre, and V. Steinberg, Europhys. Lett. **82**, 58005 (2008).

[24] D. V. Le, Phys. Rev. E **82**, 016318 (2010).
[25] F. Cirak and M. Ortiz, Int. J. Numer. Meth. Eng. **51**, 813 (2001).
[26] J. Simo and D. Fox, Comput. Methods Appl. Mech. Eng. **81**, 91 (1990).
[27] J. Marsden and T. Hughes, *Mathematical Foundations of Elasticity* (Prentice-Hall, Englewood Cliffs, NJ, 1983).
[28] R. Skalak, A. Tozeren, R. Zarda, and S. Chien, Biophys. J. **13**, 245 (1973).
[29] D. Le and Z. Tan, J. Comput. Phys. **229**, 4097 (2010).
[30] W. Helfrich, Z. Naturforsch C. **28**(11), 693 (1973).
[31] D. Le, Comput. Methods Appl. Mech. Eng. **199**, 2622 (2010).
[32] J. Stam, in *Computer Graphics (SIGGRAPH '98 Proceedings, CD-ROM Supplement)* (1998).
[33] C. Peskin, Acta Numer. **11**, 479 (2002).
[34] A. Roma, C. Peskin, and M. Berger, J. Comput. Phys. **153**, 509 (1999).
[35] D. Brown, R. Cortez, and M. Minion, J. Comput. Phys. **168**, 464 (2001).
[36] R. Lipowsky, Nature (London) **349**, 475 (1991).
[37] T. Gao and H. Hu, J. Comput. Phys. **228**, 2132 (2009).
[38] M. Zurita-Gotor, J. Blawzdziewicz, and E. Wajnryb, J. Fluid Mech. **592**, 447 (2007).